ACS APPLIED MATERIALS & INTERFACES

Research Article

www.acsami.org

Electrode Materials, Thermal Annealing Sequences, and Lateral/Vertical Phase Separation of Polymer Solar Cells from Multiscale Molecular Simulations

Cheng-Kuang Lee,[†,‡,∥] Olga Wodo,[§,⊥,∥] Baskar Ganapathysubramanian,*[,§] and Chun-Wei Pao*[,†]

[†]Research Center for Applied Sciences, Academia Sinica, 128 Sec. 2 Academia Road, Taipei 11529, Taiwan

[‡]Department of Chemical and Biomolecular Engineering, University of California, Berkeley, California 94720, United States

[§]Department of Mechanical Engineering, Iowa State University, Ames, Iowa 50011, United States

Supporting Information

ABSTRACT: The nanomorphologies of the bulk heterojunction (BHJ) layer of polymer solar cells are extremely sensitive to the electrode materials and thermal annealing conditions. In this work, the correlations of electrode materials, thermal annealing sequences, and resultant BHJ nanomorphological details of P3HT:PCBM BHJ polymer solar cell are studied by a series of large-scale, coarse-grained (CG) molecular simulations of system comprised of PEDOT:PSS/P3HT:PCBM/Al layers. Simulations are performed for various configurations of electrode materials as well as processing temperature. The complex CG molecular data are characterized using a novel extension of our graph-based framework to quantify morphology and establish a link between morphology and processing conditions. Our analysis indicates that vertical phase segregation of P3HT:PCBM blend strongly depends on the electrode material and thermal annealing schedule. A thin P3HT-rich film is formed on the top, regardless of bottom electrode material, when the BHJ layer is exposed to the free surface during thermal annealing. In addition, preferential segregation of P3HT chains and PCBM molecules toward PEDOT:PSS and Al electrodes, respectively, is observed. Detailed morphology analysis indicated that, surprisingly, vertical phase segregation does not affect the connectivity of donor/acceptor domains with respective electrodes. However, the formation of P3HT/PCBM depletion zones next to the P3HT/PCBM-rich zones can be a potential bottleneck for electron/hole transport due to increase in transport pathway length. Analysis in terms of fraction of intra- and interchain charge transports revealed that processing schedule affects the average vertical orientation of polymer chains, which may be crucial for enhanced charge transport, nongeminate recombination, and charge collection. The present study establishes a more detailed link between processing and morphology by combining multiscale molecular simulation framework with an extensive morphology feature analysis, providing a quantitative means for process optimization.

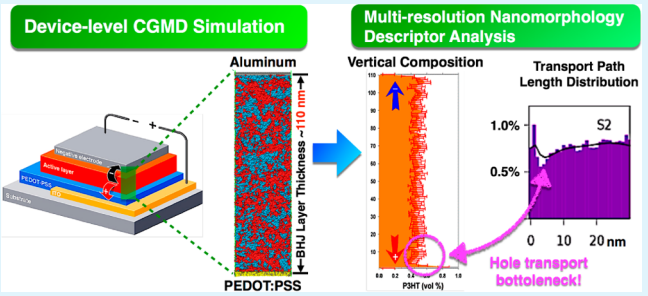

KEYWORDS: *bulk heterojunction, polymer solar cells, coarse-grained molecular simulations, nanomorphology, vertical phase segregation, thermal annealing, electron/hole transport*

1. INTRODUCTION

Bulk heterojunction (BHJ) polymer solar cells (PSCs)[1−11] are promising candidates for the production of renewable energy because of their low production costs, high mechanical flexibility, and light weight.[10−13] The photoactive layer of BHJ PSCs comprises a nanoscale, interpenetrating network of two different materials, electron donor and electron acceptor materials. Electron donor materials are usually semiconducting polymers such as poly(3-hexylthiophene) (P3HT), whereas electron acceptor materials are usually materials with high electron affinity such as [6,6]-phenyl-C61-butyric acid methyl ester (PCBM). When the BHJ layer absorbs incident photons, excitons are generated (primarily) within the electron donor domains; these excitons diffuse toward the electron donor/acceptor interface and dissociate into free electrons and holes, which are transported to their respective electrodes to generate the photocurrent. Hence, the three-dimensional organizations of the BHJ layer are critical for the overall device performance.[1−11]

In a typical fabrication procedure of bulk heterojunction polymer solar cells using thermal annealing, the electron donor/acceptor solution is first spun-cast onto the bottom electrode (usually PEDOT:PSS anode) and dried; subsequent thermal annealing can be either carried out before deposition of top electrode (preannealing), or carried out after (top) electrode deposition (postannealing). During the annealing processes, phase separation between electron donor and acceptor takes place in both vertical and lateral dimensions

Received: May 20, 2014
Accepted: November 5, 2014
Published: November 5, 2014

   dx.doi.org/10.1021/am506015r | ACS Appl. Mater. Interfaces 2014, 6, 20612−20624

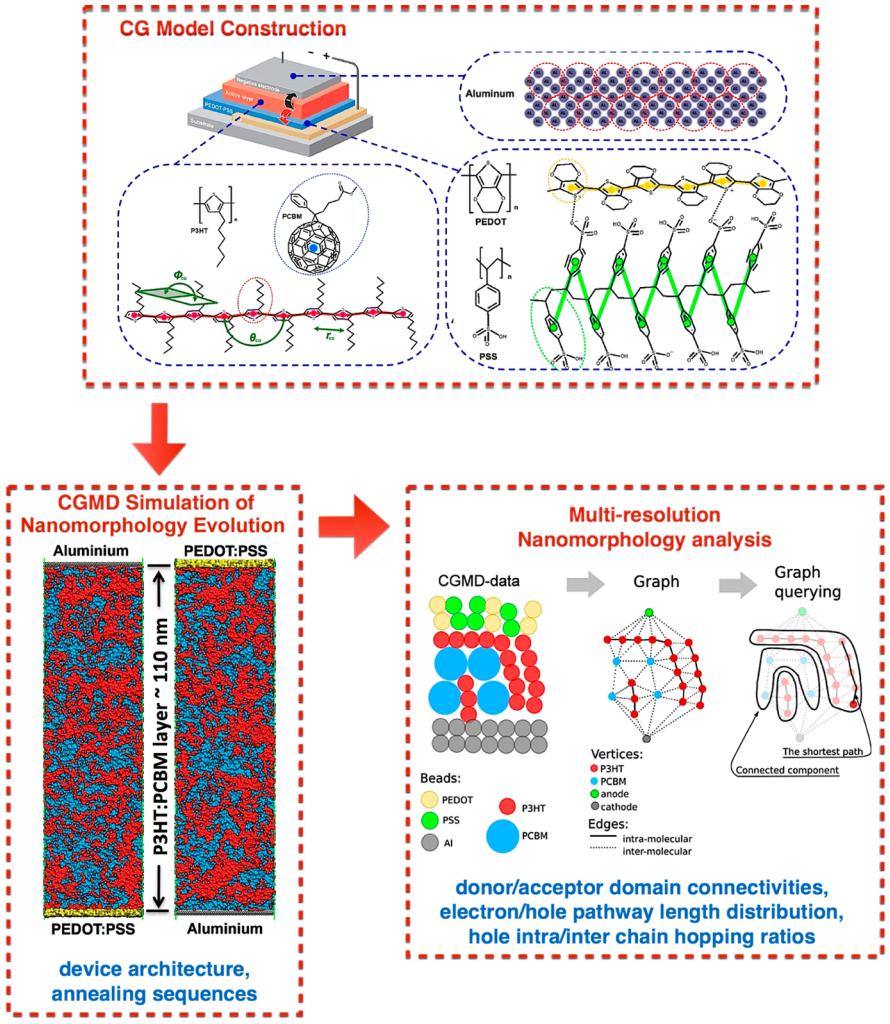

Figure 1. Schematics of the multiscale molecular simulation/characterization platform developed in the present study. Upper panel: CG model constructions for PEDOT:PSS anode, P3HT:PCBM BHJ layer, and aluminum cathode. Lower left panel: CGMD simulation of bottom electrode/P3HT:PCBM/top electrode stacking under various device architecture (left panel, standard; right panel, inverted). Lower right panel: multiresolution morphological descriptor analysis based on graph theory.

and the BHJ layer evolves. It has been demonstrated that for P3HT:PCBM blends, postannealing blends have better performance than preannealing blends,[1−7,10] which suggests that the thermal annealing sequence could play an important role in the vertical and lateral phase separation in the BHJ layer. In addition, it has also been demonstrated that PSCs fabricated with inverted device architecture, that is, using cathode as the bottom electrode instead of anode, can promote device performance, which once again suggests that device architecture can affect BHJ blend morphologies.[6,14] Therefore, comprehensive insights into the correlations between processing conditions and resultant BHJ organizations at the device level are crucial for nanomorphology control to further understand and enhance device performance.

Although the importance of the BHJ organization is widely recognized as critical to device performance, experimental characterization of the vertical and lateral organizations of the BHJ layer to understand this effect is quite challenging. Recent X-ray photoemission spectroscopy (XPS),[15] neutron reflectivity (NR),[16] and in situ ellipsometry[17] experiments have revealed the vertical composition profile of preannealed (i.e., annealed before top electrode deposition) P3HT:PCBM blends. The vertical composition profiles of both pre- and postannealed P3HT:PCBM blends have been revealed by dynamic secondary ion mass spectrometry (DSIMS)[18] and near-edge X-ray absorption fine structure spectroscopy (NEXAFS)[19] combined with the reversible delamination techniques.[20,21] These experimental studies indicated the preferential segregation of P3HT chains toward the free surface. However, although very insightful to assess preferential segregation, composition profiles along BHJ film thickness cannot be correlated with hole/electron transport path percolations. BHJ nanomorphological imaging with molecular level resolution in three dimensions, on the other hand, would provide such level of detail. When quantitatively analyzed, such 3D data would allow us to examine the charge carrier pathway both in the vertical/lateral directions. Nevertheless, this is extremely difficult even with current state-of-the-art experimental characterization tools.

Molecular simulations are a very promising approach to provide insights into BHJ morphologies that are as yet difficult to be revealed from experiments. Recent all-atom molecular dynamics (MD) simulation has revealed the phase separation processes between P3HT and fullerenes with atomistic scale resolution;[22] however, all-atom MD simulations are computationally intensive, thereby limiting both the spatial and the temporal scales explored. Instead of using all-atom MD

simulations, in which the degrees of freedom of all atoms in the system are considered, coarse-grained (CG) MD simulation can significantly reduce the total system degrees of freedom by coarsening several atoms into one coarse-grained bead to extend the spatial scale of MD simulations. Thus, CGMD simulations provide insight at the scales difficult to access using experiments and that are also challenging to obtain at the time scales typical for all-atom MD simulations. Note that CGMD simulations speed the phase separation processes because of the smoother potential energy surface resulting from smearing out atomistic details, which accelerates the dynamics of the system.[23,24] CG models are usually constructed on the basis of trajectories or energetics from all-atom MD simulations of smaller system of interests.[23] Recently, several CG models of P3HT:fullerene system have been developed for studying BHJ morphology evolution with system size compatible with experiments.[25,26] In addition to deterministic MD simulations, stochastic Monte Carlo (MC) is another powerful method to investigate the BHJ morphology at/close to equilibrium in solution,[27,28] which could hold the key toward studying long-term morphology evolution. However, all of these aforementioned computational studies focused on the BHJ morphologies in the bulk; that is, the top and bottom electrodes were not taken into account. In this work, we make a first step to close this gap. Furthermore, we additionally supplement the analysis by detailed, quantitative analysis of the morphological properties, rarely reported by other studies.

In the present study, we developed a multiscale molecular simulation framework that can both simulate and quantitatively analyze the nanoscale phase separation in both vertical and lateral dimensions of the BHJ PSC at device level, simulation system including anode, BHJ layer, and cathode. The work flow of the computer experiment/characterization framework is depicted in Figure 1. A coarse-grained (CG) molecular model comprising anode (PEDOT:PSS), BHJ layer (P3HT:PCBM), and cathode materials (Al) is constructed on the basis of all-atom molecular dynamics (MD) simulations, see the upper panel of Figure 1; this CG model is capable of simulating the morphological evolution of the BHJ layer at the device level with BHJ layer thickness up to 120 nm, which is similar to typical BHJ film thickness, under various device architectures and thermal annealing sequences (e.g., pre/postannealing), see the lower left panel of Figure 1. We subsequently perform morphological characterization based on graph theory to quantitatively analyze the nanoscale morphological details in the BHJ layer and identify effects of processing, see the lower right panel of Figure 1. Our CGMD simulations indicate that thermal annealing sequence has a noticeable impact on the vertical phase segregation of the BHJ layer. When the BHJ layer is annealed before the deposition of the top electrode (the preannealing process), a thin P3HT-rich layer is formed (at the top) regardless of the bottom electrode material. This observation is consistent with recent experiments.[6,15−19] Surprisingly, subsequent morphology descriptor analysis indicates that the formation of P3HT-rich surface layer during thermal annealing has negligible effects on the overall P3HT/PCBM domain connectivity. However, the enrichment zone (followed by a depletion zone) does affect the electron/hole transport pathway length toward electrodes. This is an important morphological feature as the longer charge carrier transport pathway is not favorable for PSC applications due to an increase in charge carrier recombination probability. Additionally, our simulations indicate that the thermal annealing sequence changes the fraction of intramolecular versus intermolecular transport along the pathways, which is crucial for the effective hole mobility. Hence, the present study presents a versatile, multiscale molecular simulation platform, which can be employed to investigate BHJ nanomorphologies. Our platform provides insights into morphological properties that are difficult to currently explore experimentally. This can potentially enable linking device fabrication conditions and resultant BHJ nanomorphologies. Note that this multiscale simulation platform can be readily extended to investigating the BHJ nanomorphologies of newly synthesized donor/acceptor materials to help experimental teams reduce costs in fine-tuning device fabrication conditions. Finally, in addition to CGMD simulations, the CG model for PEDOT:PSS/P3HT:PCBM/Al developed in the present study can potentially be extended to other molecular simulation methods to sample the BHJ morphologies close to equilibrium or in solution (to study long-term morphology evolution, solvent annealing processes).

2. SIMULATION DETAILS

To perform device-level CGMD simulations of BHJ PSC, we construct CG models that take all components of the BHJ PSC into account. Figure 1 schematically displays the typical device architecture of the BHJ PSC (upper left panel), and the chemical structures of the materials of each component layers. The CG model for the BHJ layer material, P3HT and PCBM molecules, has been constructed in our previous study of the bulk phase separation of P3HT:PCBM blends.[24] This CG model has been applied to investigating an ultralarge-scale (ca. $128 \times 128 \times 128$ nm^3) P3HT:PCBM phase separation process in the bulk using the Titan supercomputer.[25] The P3HT persistence length from this CG model was 3.3 nm,[24,25] which is in good agreement with experiment.[29] For miscibility between P3HT and PCBM, the Flory interaction parameter χ between P3HT and PCBM computed from the CG model employed in the present study was 0.92 ± 0.1,[25] which is also in good agreement with experiment ($\chi = 0.86$).[30] Finally, the structure factors computed from the P3HT:PCBM CG model employed in the present study were once again in good agreement with small-angle neutron diffraction experiments.[25,31] Hence, the CG model employed in the present study is capable of reproducing important morphological aspects also observed experimentally. In the following, we will briefly describe the CG models for the anode material (Al) and cathode material (PEDOT:PSS).

A. CG Model for Aluminum Electrode. The CG model for Al anode is constructed by mapping an atomistic model of FCC Al slab with given size (ca. $32 \times 32 \times 2$ nm^3) into a slab comprising CG particles, see the schematic figure displayed in Figure 1. In this CG model, each CG bead contains approximately 10 Al atoms, and the sizes of the CG beads are compatible with those of the CG P3HT/PCBM beads. The CG interaction potential between Al CG particles can be easily obtained by fitting the CG potential energy surface between two Al CG slabs with slab separation r, $U^{\mathrm{CG}}(r)$, to reproduce that computed from fully atomistic MD (AMD) calculations, $U^{\mathrm{AMD}}(r)$, by minimizing the following penalty function:

$$f_k = \int_0^{\mathrm{cutoff}} (U^{\mathrm{AMD}}(r) - U_k^{\mathrm{CG}}(r, \{p_n\}))^2 \, \mathrm{d}r \quad (1)$$

with respect to CG Lennard-Jones parameter set $\{p_n\}$ using simplex optimization. The optimized Lennard-Jones parameters

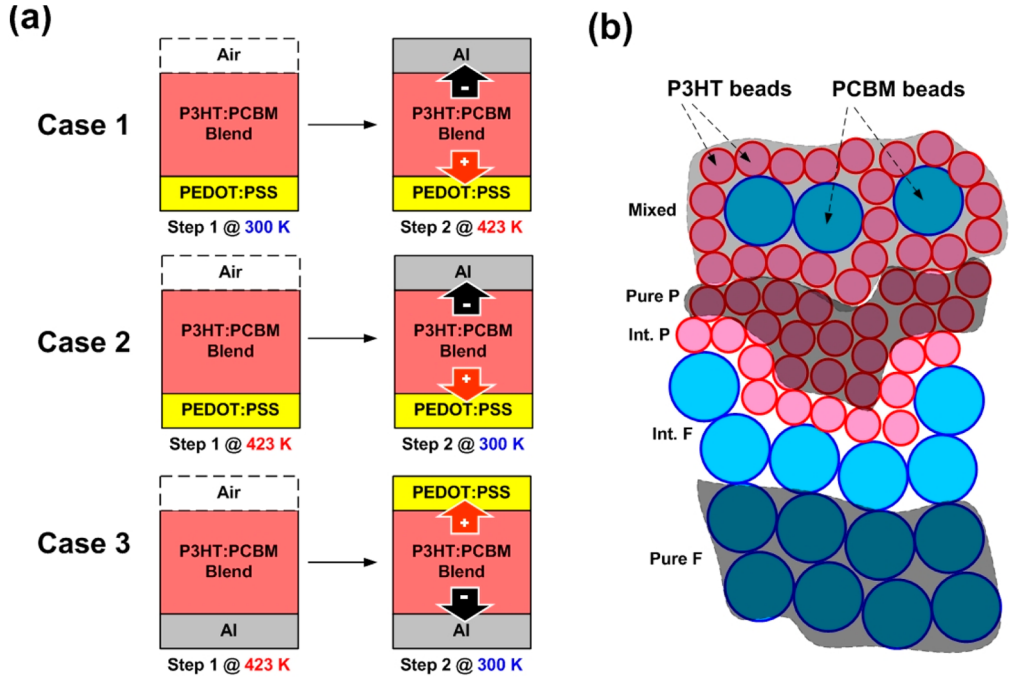

Figure 2. (a) Three different device fabrication protocols investigated in the present study; (b) beads identified as pure, mixed, or interfacial regions in the morphology of P3HT:PCBM blend, where "pure P" and "pure F" indicate pure phase of polymer P3HT and pure phase of fullerene derivative PCBM, "int. P" and "int. F" indicate interfacial regions of polymer phase and interfacial regions of fullerene derivative phase, and "mixed" indicates mixed phase of P3HT and PCBM.

for CG model of Al electrode are compiled in Table S1 of the Supporting Information. The fitted CG potential can successfully reproduce the potential energy surface between two Al slabs from AMD calculations, see Figure S1 of the Supporting Information. The CG interaction potentials between Al CG particles and P3HT/PCBM CG particles are obtained by using the mixing rule. To examine the reliability of the cross CG pair potentials, two separate simulations were carried out to compare the RDFs of P3HT monomers or PCBM molecules surrounding a slab-like aluminum electrode by the AMD and CG simulations. The RDFs from CG pair potentials derived from mixing rules are in excellent agreement with those from AMD simulations, see Figure S2 of the Supporting Information.

B. CG Model for PEDOT:PSS Anode Layer. In fitting the CG force fields for PEDOT and PSS chains, we employed the structural-based scheme similar to the scheme we used in fitting the CG force field for P3HT and PCBM in our previous study.[24,32] In this scheme, each PEDOT or PSS repeated unit (region enclosed inside the yellow- or green-dashed line in the upper panel of Figure 1) is mapped into a CG bead (colored in yellow or green) centered at the individual thiophene or aromatic ring. The CG force fields are fitted using simplex optimizations to reproduce structural properties [e.g., radial distribution function (RDF), CG bond length, bond angle, and dihedral angle distribution] of CG degrees of freedom computed from AMD simulations of the system of interest with smaller size. The details of the fitting procedures can be found elsewhere.[24,32] The optimized potentials parameters are compiled in Table S1 of the Supporting Information. The fitted CG force field for PEDOT and PSS can successfully reproduce the structural properties computed from AMD simulations, see Figure S3 (intramolecular CG degrees of freedom) and Figure S4 (intermolecular CG degrees of freedom, RDFs) of the Supporting Information. In addition, to take the ionic interaction between PEDOT and PSS into account, we add positive and negative charges into CG beads of PEDOT and PSS, respectively, see the upper panel of Figure 1. The ratio of charged to neutral CG beads is set to 1:3 for each PEDOT and PSS chain to comply with experimental observations.[33,34] The PEDOT:PSS electrode in the CG representation employed in the present study is displayed in Figure S5 of the Supporting Information. From Supporting Information Figure S5 we observe flexible PSS chains (colored in green) winding around rigid PEDOT chains (colored in yellow) by the ionic bonds, which is consistent with experimental observations. In subsequent CGMD simulations, the MD package, DL_POLY_4, was employed.[35] The system temperatures and pressure were controlled at 300 K/423 K and 1 atm, respectively, by using a Nosé−Hoover thermostat and barostat. The simulation time step was set to 5−10 fs in CGMD simulations. The CGMD simulation time for each step in Figure 2a was 20 ns. Nevertheless, as mentioned above, in CGMD simulations, the system dynamics are "accelerated" because of the smoother potential energy surface as compared to that of all-atom MD. To get insight into the time-scaling between CGMD and the underlying atomistic systems, we have to compare system characteristic time scales (e.g., P3HT end-to-end correlation time) from CGMD and respective all-atom MD simulations. The time-scaling factor of the P3HT:PCBM CG model in the present study was 15.6,[24] implying that the CGMD simulation time in the present study is of the order of microsecond. Periodic boundary conditions were applied only to the lateral directions, x and y directions, so as to simulate the effects of free surface in the z direction.

C. Graph-Based Morphology Analysis. To compare the CG morphology obtained by processing with various protocols, we use our graph framework to extract physically meaningful

Table 1. Concentration of Domains, and Fraction of Bead Identified as Pure, Mixed, or Interfacial Regions in the Morphology[a]

	case 1		case 2		case 3	
phase	step 1	step 2	step 1	step 2	step 1	step 2
pure P	5.7%	8.6%	15.2%	13.7%	14.8%	12.8%
int. P	21.1%	24.0%	27.9%	27.3%	27.2%	27.1%
pure P + int. P	26.8%	32.6%	43.1%	41.0%	42.0%	39.9%
pure F	0.2%	0.3%	0.8%	0.6%	0.7%	0.7%
int. F	1.2%	1.7%	3.5%	3.1%	3.3%	3.0%
pure F + int. F	1.4%	2.0%	4.3%	3.7%	4.0%	3.7%
mixed	71.7%	65.3%	52.3%	55.2%	53.8%	56.3%

[a]Fraction by total number of beads in the morphology.

morphological features that are relevant for the photovoltaic phenomena in a BHJ.[36−38] We first convert the CGMD point cloud 3D data into a labeled, weighted, undirected graph and then use standard graph-based algorithms to calculate and quantify morphology features. While we give a brief overview of the framework here, more details can be found elsewhere[36−38] and in the Supporting Information. The lower right panel of Figure 1 shows a schematic overview of the graph-based framework. Beads from the CG-simulations are naturally represented as vertexes with a label (here we use colors to characterize various labels) denoting the type of bead. Neighboring beads are connected via edges. Each edge is classified as an "intramolecular" or "intermolecular" edge. Neighboring beads belonging to the same polymer chains are connected by intramolecular edges (bold lines in the middle of the lower right panel of Figure 1), while adjacent neighbors are connected by intermolecular edges (dotted lines in the middle of the lower right panel of Figure 1). Each edge is also associated with a weight that expresses the physical distance between beads and is used to compute path lengths. To facilitate analysis, two meta-vertexes are added to the base graph and represent the anode and cathode. The conversion of the CGMD-data into a graph preserves all of the topological and geometric information about the internal structure, and local connectivity between individual beads. We focus on extracting two types of information from the graph, connectivity and the shortest paths. We use standard graph-based algorithms such as finding connected components and Dijkstra algorithm.[39,40] We use the connected component concept to isolate coherent subdomains of morphologies that consist of one type of bead only (see the lower right panel of Figure 1). This type of information is used to investigate the connectivity of domains to electrodes. We exploit Dijkstra algorithm,[39,40] in turn, to find the shortest path in the graph. For example, for each polymer bead, we find the shortest path to the anode where the path consists of polymer beads only. In this way, we estimate the shortest path that a hole would need to take to reach the electrode. By subsequently quantifying specific features of the path, we gain insight into usefulness of such paths in the photovoltaic process. In particular, we focus on path length, fraction of intramolecular hops, and path balance. We also quantify the first layer of beads directly adjacent to the electrode to unravel propensity toward good charge collection. These descriptors enable gaining multi-resolution insight (focusing on various scales of interest) into the morphological features, which are subsequently used to assess the effect of processing on the BHJ and to compare various configurations. This framework has several important advantages in the context of the work presented here. First, CGMD-data naturally translate into a graph, with no intermediate conversion into voxel-wise representation. Next, information such as intra- and intermolecular paths can elegantly enrich quantification providing a more detailed path analysis. It should be noted that such imaging and quantification is currently highly challenging using purely experimental approaches. Therefore, this unique combination of CGMD data and a graph-based method allows unprecedented opportunity to gain more understanding into the morphology. Finally, the graph-based algorithms used here are highly efficient with a total run time for a morphology consisting of about 500 000 beads taking around 5 min on a PC.

3. RESULTS AND DISCUSSION

To have comprehensive insights into the effects of electrode materials and annealing conditions on the vertical and lateral organizations of the BHJ layer, we simulated the evolution of the BHJ layer of P3HT:PCBM blends under three different processing conditions, see Figure 2a. In case 1, the P3HT:PCBM blend was first deposited on the PEDOT:PSS bottom electrode (anode); subsequent thermal annealing simulation at 423 K was carried out with the presence of Al electrode (cathode). Case 2 differs from case 1 in the sequence of thermal annealing: the P3HT:PCBM blend was thermal annealed at 423 K prior to deposition of Al electrode, thermally annealed with open surface. Case 3 has the same thermal annealing schedule as case 2 (i.e., thermal annealing prior to deposition of top electrode); however, the device architecture is inverted, and the Al electrode (anode) becomes the bottom electrode. Previous experimental studies have indicated that devices fabricated with a protocol analogous to case 1 give better performance over those fabricated with a protocol identical to case 2, while devices fabricated with inverted architecture (case 3) give higher performance than traditional configuration (case 2). The reasons causing such differences in device performance (due to annealing sequence) are as yet unclear, and we hope our CGMD simulations at the device level can help understand the reason behind these differences.

A. Region Concentration. Phase identification is a challenging problem, particularly in case of organic blends. Intense discussions continue regarding the number of phases present in a BHJ sample. Recently, an increasing number of experimental studies provide consistent evidence confirming the presence of a third phase, mixed phase in addition to the polymer-rich and fullerene-rich phases.[37,41−44] CGMD analysis provides a good way to look at phase concentration by considering the detailed neighborhood information on each individual bead. By considering the immediate neighborhood of every bead, we identify beads that are surrounded only by beads of the same type. These beads form regions that can be

considered as pure domains. We denote these beads as pure P and pure F, respectively (see Figure 2b). Next, we identify beads that have at least one pure P or pure F bead in their immediate neighborhood. This allows enumerating the beads that are directly adjacent to the pure domains, separated by one hop. We denote these beads as interfacial beads (see Figure 2b). Finally, beads that are neither pure nor interfacial are classified as mixed (see Figure 2b). This classification is admittedly coarse. Note that this is due to the fact that we assume that pure domains have no nonsimilar species neighbors, which may not be true when the domains have a small fraction of impurities. Nevertheless, this classification gives interesting insight into the morphology. In particular, by identifying beads that are surrounded by the same type of material, we find regions where nongeminate recombination is physically difficult. Table 1 displays the concentration statistics for all six samples. Interestingly, none of the samples contains any bead that would be directly adjacent to pure polymer and pure fullerene phase at the same time (not shown in the table). This is consistent with our previous analysis of experimental data (electron tomography data), where the volume fraction of the interfacial region between polymer-rich and fullerene-rich phase was smaller than 1%.[37] Note also that the samples contain a relatively high fraction of beads that we classify as pure P. Except case 1, this fraction varies from 13% to 15% of total number of beads. The value is slightly higher for steps corresponding to annealing. This suggests that annealing as the last step enhances the domain size of polymers, enabling better charge transport. Surprisingly, pure F is almost nonexistent in all samples. The reason behind this may be purely geometrical. Fullerene beads are larger in size as compared to polymer beads, and consequently the smaller polymer beads can pack in between the larger fullerene beads. Nevertheless, the information we extract from samples indicates that fullerenes are rarely surrounded purely by fullerenes. The majority of the sample is occupied by beads that have a mixed neighborhood. Among all of the samples, case 1 contains the highest fraction of beads that have mixed neighborhood that can be classified as mixed phase. Recent studies show that the presence of mixed phase can mitigate recombination by affecting the LUMO energy level of PCBM within mixed phase.[45] This may be a reason why the sample corresponding to case 1 (more than 65.3% of mixed phase) outperforms case 2 (55.2%).[1−7,10]

B. Vertical Distribution of Material along Film Thickness. The distribution of material along the film thickness is one of the basic morphological features related to device performance. Vertical heterogeneity (enrichment/depletion zones) may strongly affect the device performance as this is the direction of charge transport. For example, an enrichment layer of the donor close to the anode can improve charge collection, as it maximizes the contact area with electrode and facilitated the process. Similarly, an acceptor enrichment layer near the cathode improves the opposite charge collection. Yet any depletion zones along the thickness can create bottlenecks for charge transport, as this leads to charge accumulation, increased recombination, and deteriorating device performance.

i. Vertical and Lateral Phase Separation. Figure 3 displays the P3HT:PCBM blend morphologies (Figure 3a−c) and vertical P3HT concentration profiles (Figure 3d−f) after the first step of processing (left panels in Figure 2a). Figure 5 displays the blend and vertical P3HT concentration profiles after the second step of processing (right panels in Figure 2a).

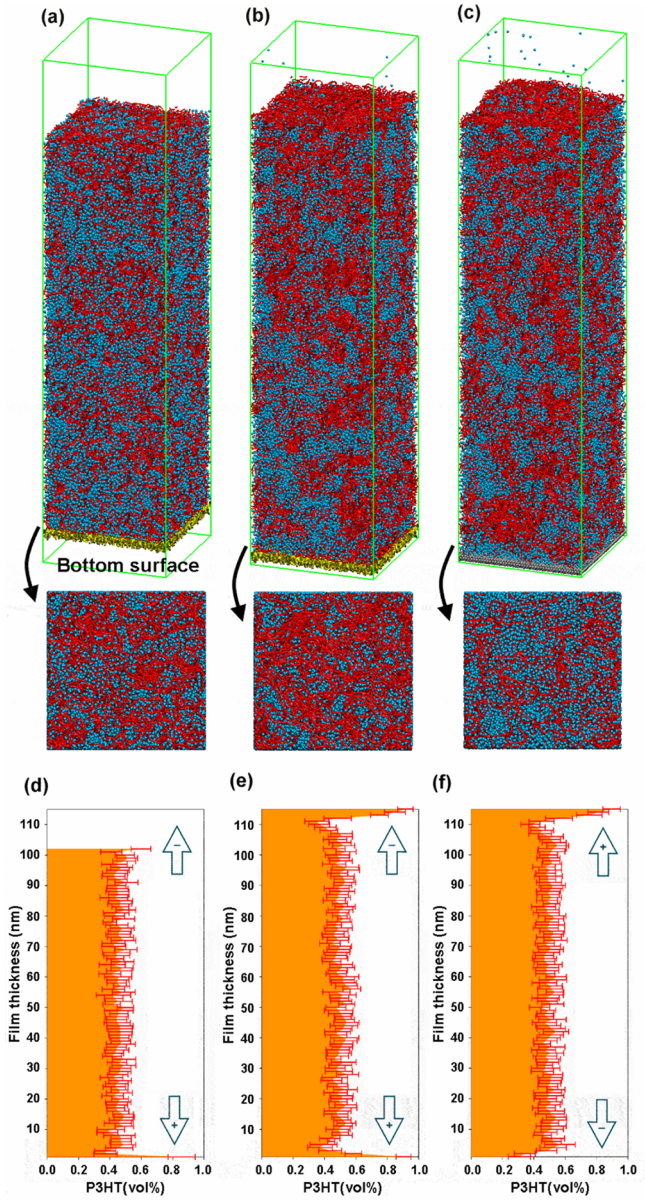

Figure 3. Morphology of P3HT:PCBM blend after step 1 in (a) case 1, (b) case 2, and (c) case 3; (d)−(f) vertical P3HT volumetric concentration profiles of the P3HT:PCBM blend after step 1 in (d) case 1, (e) case 2, and (f) case 3.

An inspection of the vertical concentration reveals the following observation related to the effects of thermal annealing on the blend morphologies. For blends processed at room temperature in the first step (case 1), no noticeable phase separation in both lateral and vertical directions between P3HT/PCBM is observed at this stage, see Figure 3a and d. When Al cathode is deposited in the second step and sample is annealed, phase separation between P3HT and PCBM takes place, as expected at the elevated temperature, see Figure 3a. Moreover, a very thin enrichment layer forms at the bottom electrodes during the first step, and an additional thin PCBM layer at the top electrode in the second step. For blends that are thermally annealed in step 1 (cases 2 and 3), however, significant phase separation in both vertical and lateral directions is already observed in the first step, see Figure 3b and c. When electrode is deposited in the second step with the system temperature set

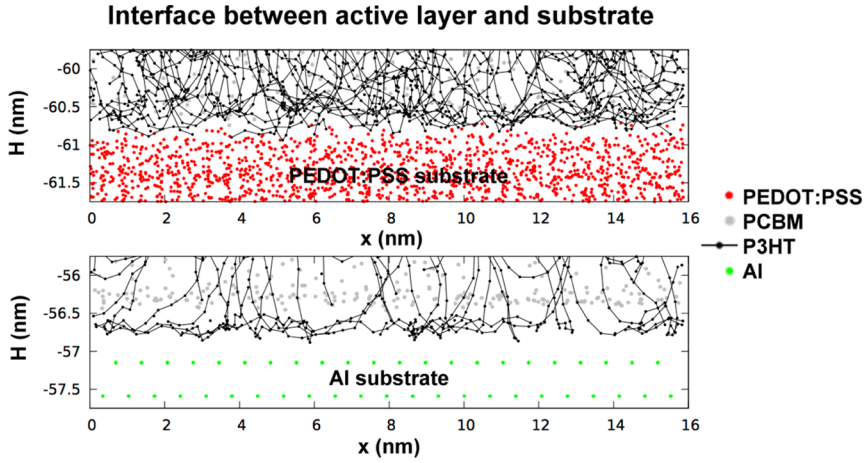

Figure 4. Interface between the substrate and the active layer PEDOT:PSS (top) and Al (bottom), plotting by the side view of the 2 nm zone close to the interface. Black dotted lines correspond to the polymer beads, while dots of other colors correspond to the bead's center of other types of molecules.

to room temperature (300 K), no subsequent changes are observed. Here, however, both top and bottom enrichment layers formed in the first step undergo further changes during the second step. We focus on these changes in subsequent analysis. Phase separation in case 1 is less pronounced as compared to cases 2 and 3. The major difference comes from the sequence of thermal annealing. In the first case, thermal annealing is performed with the top electrode already in place, while in the next two cases thermal annealing is performed before top electrode deposition. The tendency to restrain phase separation during annealing is believed to be caused by the cathode placed on top.[16] Our simulation results support this hypothesis.

ii. Formation of Polymeric Thin Enriched Layer on Top Surface. During the first step, for annealed samples (cases 2 and 3), the free surface is enriched in P3HT, see Figure 3b and c. Close examination of the vertical P3HT concentration profiles (Figure 3e and f) indicates that the surface is covered by a thin (~5 nm thick) P3HT-rich film after thermal annealing. The enrichment layer is followed by a small depletion zone. Recent XPS,[15] VASE,[46] NR,[15−18,46−49] NEXAFS,[19,50] and DSIMS experiments also indicated the existence of P3HT enrichment layer at the free surface; therefore, the vertical composition profile of P3HT from the present study is in good agreement with experiments. Lower surface energy of P3HT as compared to PCBM is usually mentioned as the reason for the thin enrichment layer formation.[6,51] Lower surface energy of P3HT tends to drive P3HT to the top surface. The absence of this layer for the room temperature prepared sample (case 1) additionally shows that preannealing may be a key factor for P3HT to drive toward free surface.

iii. Enrichment Layer Formation on Both Electrodes. As noticed above, the preannealing leads to P3HT-rich top layer formation. At the same time, the bottom surface is observed to be enriched as well already after the first step of processing, regardless of the processing temperature. However, component that builds up on the bottom surface depends on the electrode material. Samples deposited on PEDOT:PSS show P3HT enrichment layer (cases 1 and 2, see the lower panel of Figure 3a,b and d,e, notice that the PEDOT:PSS/BHJ interface is slightly P3HT-rich). The enrichment of P3HT close to PEDOT:PSS interface has been revealed from DSIMS experiments,[18] and, therefore, our CGMD simulations are consistent with experimental observations. In contrast, sample deposited on Al shows a PCBM-rich layer (case 3, see Figure 3c and f), which indicates the segregation of PCBM molecules toward Al cathode upon thermal annealing. This is again consistent with recent NEXAFS and DSIMS experiments on postannealed samples.[18] Furthermore, in Figure 4, we visualize P3HT penetration into underlying PEDOT:PSS. In this figure, we focus on a 2 nm zone around the interface between the active layer and the substrate. In case of Al substrate, there is no sign of diffusion of P3HT or PCBM into Al-layer, while for PEDOT:PSS substrate, the interface is diffused over approximately 0.5 nm distance. This may be the reason behind the easy delamination of Al-substrate reported in ref 46. Such easy delamination, on the other hand, was not observed for PEDOT:PSS substrate. References 18 and 46 hypothesized the interdiffusion of active layer and PEDOT:PSS as a potential reason for this lack of delamination. Our results support these claims by looking at individual layers close to the interface. It is interesting to notice that the affinity of PEDOT:PSS with PCBM is expected to be stronger than that of PEDOT:PSS with P3HT, because the butyric acid methyl ester group of PCBM is more polar than P3HT, thereby leading to stronger interaction with polar PEDOT:PSS. From Table S1 in the Supporting Information, the CG potential well depths (which reflects the interaction strength between CG beads pairs) between PEDOT−P3HT ($\varepsilon_{\mathrm{P3HT-PEDOT}}$), PSS−P3HT ($\varepsilon_{\mathrm{P3HT-PSS}}$), PEDOT−PCBM ($\varepsilon_{\mathrm{PCBM-PEDOT}}$), and PSS−PCBM ($\varepsilon_{\mathrm{PCBM-PSS}}$) pairs were 0.30, 0.26, 0.52, and 0.44 kcal/mol, respectively. This shows that the interaction between PEDOT:PSS and PCBM in the CG potential (which was fitted based on all-atom interaction potential) is indeed stronger than that between PEDOT:PSS and P3HT. Nevertheless, in the present study, the observed affinity of P3HT with PEDOT:PSS is noticeably higher than that of PCBM. We conclude that this can be attributed to the penetration of P3HT into PEDOT:PSS layer, see the upper panel of Figure 4. The large (ca. 10 Å) and rigid fullerene cage prevents PCBM from penetrating into PEDOT:PSS layer; in contrast, the thiophene rings of P3HT are much smaller (ca. 5 Å), and the hexyl side chain is much more flexible than fullerene cage, facilitating the penetration of P3HT chains into the PEDOT:PSS layer to strengthen the affinity between P3HT and PEDOT:PSS.

The preferential segregation of PCBM toward the Al cathode can be attributed to the attraction between P3HT/PCBM and underlying Al slab, which is implicitly encapsulated in the CG force field developed in the present study through the PCBM/P3HT-Al RDF displayed in Figure S2 in the Supporting Information. Because both P3HT and PCBM molecules are primarily comprised of carbon and hydrogen atoms, the attractive interaction between P3HT/PCBM molecules with the Al slab depends on the total van der Waals attractive interaction between carbon/hydrogen atoms in P3HT/PCBM molecules and Al atoms. Because the carbon−aluminum van der Waals attraction is much stronger than that of hydrogen−aluminum, the interaction between PCBM molecule and Al slab is stronger than that of P3HT simply because PCBM−Al slab attraction comes mostly from carbon−aluminum attraction, whereas the weaker hydrogen−aluminum attractions make substantial contribution to the P3HT−Al slab attraction through the hexyl side chain.

In general, the phase segregation of P3HT/PCBM at the cathode interface depends on the cathode material. The preferential segregation of PCBM molecules toward cathode interface has been studied experimentally for Al, ZnO, and Si cathodes.[15,16] Experimental observations from both in situ ellipsometry[17,19,46] and NEXAFS[17,19,46] indicate that the affinity of PCBM toward silica is not as strong as that toward Al and ZnO. Weaker affinity of Si could be attributed to the hydroxyl groups on silica surfaces. Another explanation is based on the link between enrichment and substrate surface energy. In ref 46, it has been shown that by consistently changing the material of the substrate into one with lower surface energy, the enrichment of PCBM also systematically decreased. The affinity of P3HT/PCBM with various cathode materials is an important question worth exploring, which we plan to investigate in the future using this framework.

Similar to the free surface, behind the bottom enrichment layer a local depletion zone forms. This zone is clearly manifested in Figure 3e as a double well shape. A similar double well shape of vertical profile was also reported experimentally.[37] Substrate-induced phase separation was hypothesized as a mechanism behind this vertical distribution.[15,46] In ref 17, the extent of the zone was found to be comparable to the characteristic wavelength, 80 nm for P3HT:PCBM. However, in all of our samples, the extent of the enrichment layer is much smaller. We attribute these local changes to short-range attraction with the substrate. We believe that this enrichment zone may be a result of the quick uptake of P3HT from the neighborhood due to affinity toward PEDOT:PSS. The adjacent depletion zone is the result of slow diffusion from the bulk that does not compensate for quick migration of preferred component toward the electrode. The trend to create preferential enrichment zone on the bottom electrode followed by a (disadvantageous) depletion zone is maintained during the second step of processing. Figure 5 displays the blend morphologies (Figure 5a−c) and vertical P3HT concentration profiles (Figure 5d−f) after the deposition of the top electrodes. Note that blends in case 1 were thermal annealed at 423 K in this step, whereas the system temperatures were set to room temperature (300 K) for cases 2 and 3. In case 1, an initially small enrichment layer of P3HT enlarges slightly at the anode. In two other cases, the extension of the enrichment zone is not changed (system temperatures are set to room temperature during the second step; therefore, it is not surprising that there are no noticeable changes in bottom

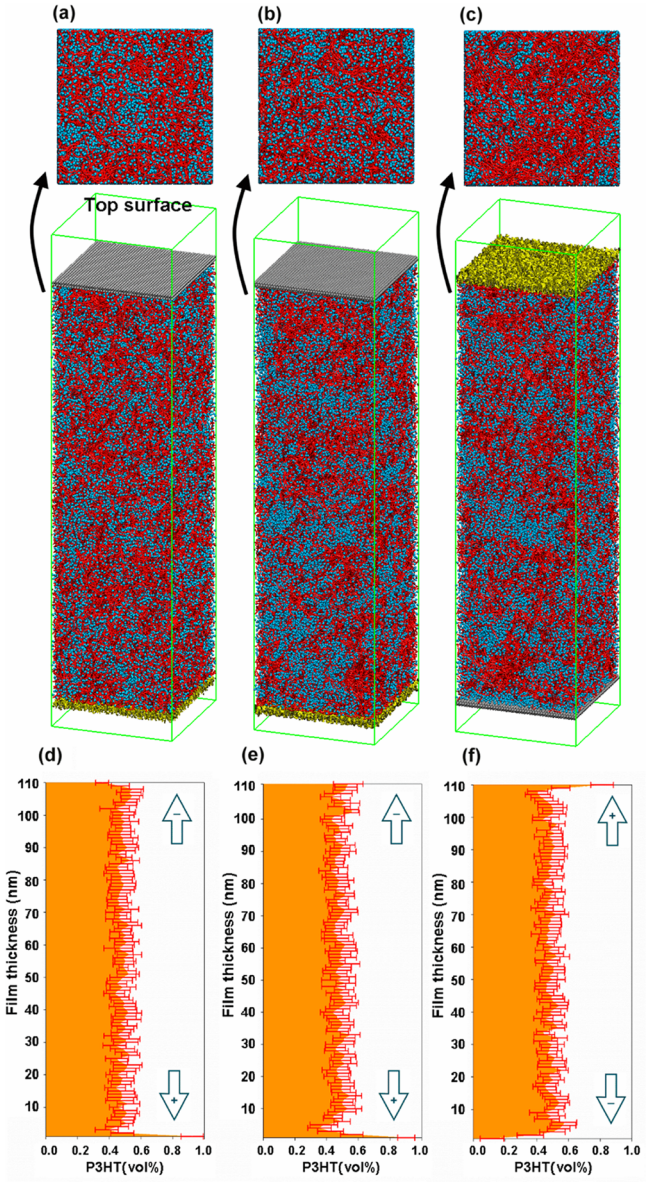

Figure 5. Morphology of P3HT:PCBM blend after deposition of the top electrode (step 2) in (a) case 1, (b) case 2, and (c) case 3; (d)−(f) vertical P3HT volumetric concentration profiles of the P3HT:PCBM blend after step 2 in (d) case 1, (e) case 2, and (f) case 3.

enrichment layer during the second step). The top surface, however, undergoes major changes in the second step, which involves the top electrode deposition. In cases 1 and 2, Al cathode is placed on the top, while in case 3, PEDOT:PSS anode is deposited on the top surface. As a consequence, in case 1, on an initially neutral surface (after first step), a thin PCBM-rich layer forms close to the BHJ/Al interface (see Figure 5d), manifesting the affinity of PCBM toward Al. In case 2, the Al cathode attracts PCBM toward the top surface; however, we believe that there is most likely not enough time to form a clear enrichment layer. Deposition process is carried out at room temperature, and the mobility of PCBM is lower as compared to case 1. In addition, the P3HT-rich layer formed during the first step needs to be counteracted by PCBM accumulation. As a consequence, for case 2, the P3HT-rich layer formed during the first step only shrinks in the second step. Finally, in case 3, the P3HT-rich layer formed during the

first step is still preserved; however, its extent is decreased slightly (as seen in the vertical profiles of Figures 3f and 5f). It is important to notice that, regardless of processing, a preferential enrichment zone forms close to the electrode in most cases. This emphasizes the importance of the proper choice of the electrode material as either a means to promote enrichment layer formation or to counteract the unfavorable layer formation (as in case 2-step 2). In principle, the donor affinity toward anode material is beneficial for hole collection, because it leads to increased contact area and facilitates charge collection. However, this comes at a price of the depletion zone formed just behind the outer layer that affects the quality of paths to the electrodes. This interplay is analyzed in the next section.

iv. Contact with the Electrode. As a next step of multiresolution morphology analysis, we quantify the layer of the BHJ domain adjacent to the electrodes. Table 2 details the fraction of P3HT adjacent to the anode, and the fraction of PCBM adjacent to the cathode. Note that the fraction is defined in terms of the total number of beads adjacent to the electrode. Interestingly, the protocol of anode placement does not affect the contact area with P3HT. The values are in the comparable range between samples (within a 10% range). In contrast, PCBM contact area with cathode is highly sensitive to the protocol applied and can even be doubled. In particular, our studies indicate appreciable contact area improvement when blend is deposited on cathode in the first step. On the other hand, when cathode is deposited in the second step as top electrode, its strong affinity toward PCBM first needs to counteract the P3HT-layer formed in the first step. It is important to mention that this analysis, with the virtue of being computational, is not affected by the problem of Al electrode removal process. This is often mentioned as a hindrance in the context of similar experimental measurements.[52]

Table 2. Composition of the BHJ Adjacent to the Electrode[a]

	case 1		case 2		case 3	
electrode	step 1	step 2	step 1	step 2	step 1	step 2
f^{P}_{an}	81%	84%	89%	88%		91%
f^{E}_{cath}		23%		26%	45%	44%

[a] f^{P}_{an}: Fraction of P3HT bead on anode. f^{E}_{cath}: Fraction of PCBM bead on cathode. Fractions are computed with respect to total number of beads directly adjacent to respective electrode.

C. Connectivity to Electrodes. Holes and electrons require continuous paths with direct connection toward the respective electrode to be collected and contribute to current generation. We investigate the fractions of polymer and fullerene beads that are connected to anode and cathode, respectively. All morphologies show perfect connectivity to electrodes regardless of processing, as detailed in Table 3. Both polymer and fullerene regions are 100% and 99% connected to the relevant electrode, respectively. This overall high connectivity can be explained via percolation arguments because the blend consists of similar volume/weight of P3HT and PCBM. Such blend ratios are above the percolation threshold, and high connectivity is consequently expected and has been reported consistently in other studies.[37,53] At the same time, this high connectivity is remarkable taking into account the thin depletion layers formed close to the electrodes. Such a potentially blocking layer could affect the overall connectivity, but our analysis quantitatively shows that this is clearly not the case. A connected component analysis revealed that the polymer beads constitute a single large interconnected component, without any isolated chains. The fullerene beads, on the other hand, constitute more connected components (Table 3). Some fullerene beads are fully surrounded by polymer beads and constitute small connected components that usually do not have direct connection to the electrode. In case of case 3-step 1, there are as many as 350 regions that are isolated. Nevertheless, the domain size of these regions is marginal, less than 1% of the total number of beads. The remaining beads construct large components that are connected to cathode. This indicates that the morphology is indeed well interconnected in the bulk as desired for good performance. Moreover, looking into the statistics of connected components provides insight into the importance of the thin layers close to the electrodes, which so far have not been well understood.[16] As long as one large polymer component is in contact with the electrode, regardless of the partially blocking layer, the overall connectivity remains high. This is because the depletion layers do not cover the entire surface, ensuring that the connectivity of both types of domains to the electrode is high for all samples. These results are consistent with our previous results related to three-phase, three-dimensional morphology visualized with electron tomography.[37] This observation is also consistent with previous experimental work,[19] where authors speculated that as long as contact area between fullerene and cathode is nonzero (even as low as 3%), it enables electron extraction. However, the quality of percolation pathways can be affected by the partially blocking layer exposed by vertical segregation profile. We focus on this aspect in subsequent sections.

D. Quality of Percolation Pathways toward Electrodes. While high connectivity is a necessary condition for charge transport to be possible, there are additional features that must also be considered in the context of morphology. One such

Table 3. Connectivity Statistics[a]

	case 1		case 2		case 3	
electrode	step 1	step 2	step 1	step 2	step 1	step 2
f^{P}_{an}	100%	100%	100%	100%		100%
CC^{P}_{an}	1	1	1	1		1
f^{E}_{cath}		99.7%		99.4%	99.2%	99.4%
CC^{E}_{cath}		5		2	1	4
CC^{F}	65	142	332	269	351	279

[a] f^{P}_{an}: Fraction of polymer beads connected to anode. f^{E}_{cath}: Fullerene beads connected to cathode. CC^{P}_{an}: Number of polymer connected components connected to anode. CC^{E}_{cath}: Number of fullerene connected component connected to cathode. CC^{F}: Total number of fullerene connected components in the sample.

characteristic is the path length that charges take to reach the respective electrode. The longer is the path, the higher is the probability of recombination, due to limited lifetime or interaction with opposite charges. Furthermore, in case of hole transport, polymer chain orientations play an important role. Orientations that enable transport along the polymer backbone rather than transport across polymer chains are preferable due to the higher mobility along the chain as compared to hopping across chains.[54] To assess the quality of pathways, the shortest pathway from every bead to the respective electrode is determined. These pathways consist of only polymer beads for hole transport to the anode, and consist of only fullerene beads for electron transport to the cathode. For each such pathway, the path lengths are computed. An analysis of the shortest paths provides insight into the morphology with respect to percolation pathways. We utilize a multiresolution analysis strategy by first looking only into paths that are shorter than 30 nm, then considering all pathways, and finally distinguishing between interchain and intrachain transport.

i. Length Distribution of the Shortest Pathway. We first focus on the distribution of path lengths that are shorter than 30 nm to assess the effect of electrode placement in the zone directly adjacent to electrode. Figure 6a and b displays the histogram of P3HT and PCBM path length for all analyzed cases. Histograms are constructed with a bucket size of 1 nm, and fractions are computed with respect to the total number of beads of a type. Note that for case 3-step 1, there is no anode deposited; therefore, P3HT paths are not investigated. Similarly for PCBM, for cases 1 and 2 at step 1, there are no histograms plotted, because for these samples there is no cathode deposited. The first set of values in the histograms corresponds to the shortest paths in the morphology. These are the paths that are adjacent to the respective electrodes. The higher is the fraction of P3HT or PCBM in the first layer (Table 1), the higher is the fraction corresponding to very short paths in the histogram. For example, for case 3, the fraction of PCBM in contact with cathode is nearly doubled as compared to case 1 and case 2. Note that the exact values do not match though, because the fractions are computed with respect to various quantities (total number of beads in the first layer and total number of P3HT/PCBM beads in the sample). Looking at values slightly larger than 1 nm reveals the effect of the enrichment layer (Figure 6a and b). In all cases, there is a decrease with characteristic wells. The location and depth of the characteristic well differ between samples, and are strongly correlated with the thin local enrichment layer (Figures 3 and 5) followed by a depletion zone. Beads located behind such a layer require a more torturous path to reach the electrode. The more pronounced is the depletion layer, the larger is the number of beads affected. This is especially illustrated by looking at the PCBM paths to cathode in case 3, which are clearly more torturous with several wells in the histograms. At the same time for case 1-step 2, PCBM path length is more homogeneous close to cathode. Interestingly, for all samples, the first well in the histogram has a comparable path length of 3−5 nm. This is consistent with the vertical profile close to both electrodes. This suggests that the direct influence of the enrichment/depletion zone is comparable for all cases. The only exception is the PCBM pathway in case 3, where the well is manifested around 5−6 nm. In case 3, there are two additional wells in the histogram, which could be an indicator for bottlenecks in charge transport, with the number of wells

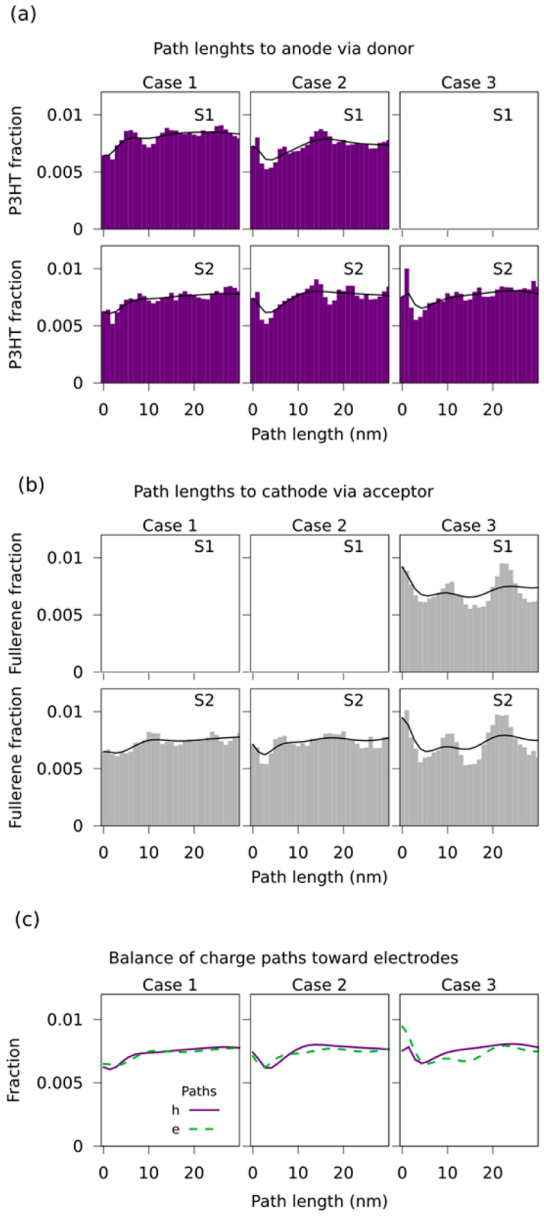

Figure 6. (a,b) Histogram of distances from any P3HT (a) or PCBM (b) bead to their respective electrodes via donor (a) or acceptor (b) domains, and (c) path balance of hole and electron paths.

being a signature of charge transport bottleneck. At the same time, homogeneous histogram of path length can be considered as an indication for high percolation of charges. The histograms (Figure 6a and b) reveal that the best pathway properties are for case 1 when taking both P3HT and PCBM into account, with case 3 having the worst properties. This observation emphasizes the importance of having a high contact area with relevant electrode as well as the absence of any depletion zone behind it. Finally, comparison of pathway lengths between steps in each case does not reveal any clear differences. For cases 2 and 3, histograms for step 1 are very similar to those for step 2. After the first step, the placement of the top electrode does not significantly affect the pathways to the bottom electrode. This is not surprising as top electrode deposition is done at room temperature, and there is not enough driving force for subsequent evolution. However, in case 1, the thermal annealing during the second step does affect P3HT path

length distribution. The fraction of beads with short path lengths increases, and the second well disappears. Migration of the P3HT toward the anode is the most likely cause. Interestingly, the extent of the influence/depletion zone until the first well remains the same, as displayed in Figures 5a,d and 6a. In summary, the worst length distribution of both PCBM and P3HT pathways is for case 3, with the best path length distribution for case 1.

ii. Path Balance. Charge transport and collection is a complementary process. If only one type of pathway is of high quality, the overall current generation may be severely affected by bad path balance due to charge buildup at the electrode. Therefore, it is worthwhile to look into the balance of paths. Here, we focus on path balance in terms of compatibility between pathway length distributions. Figure 6c plots the balance of the short-range pathways between hole and electrode paths (path lengths <30 nm). We construct a histogram of pathways lengths (Figure 6a and b), fit them with splines, and overlay them. Among all three samples, the one annealed with both electrode deposited, case 1, shows the best path balance. While for all samples clear wells are present in hole and electron path length histograms, only for case 1 are the characteristics of the both types of pathways complementary. In case 1, both fitted histograms are nearly perfectly overlaid. In contrast, the worst balance between paths is observed for case 3, indicating that this can be one of the potential bottlenecks for charge transport and collection. Superior path balance for case 1 can be one of the reasons for the reported improved performance via a postannealing protocol.[1−7,10]

iii. Intra- and Intermolecular Transport along Hole Pathways. Recent work suggests that interchain transport and intrachain transport operate at different time-scales, and that this distinction can be used to qualitatively explain a large body of experimental work.[54] In ref 54, by distinguishing between (slow) interchain and (fast) intrachain transport, the authors were able to explain the multiscale nature of mobility that has been reported in a variety of materials.[55,56] We use this as a motivation to distinguish between interchain and intrachain regions in hole pathways. Our graph-based method allows labeling edges as intramolecular if neighboring beads belong to the same polymer chain. We subsequently count the intra- and intermolecular segments along the shortest pathways toward anode and report the fraction of that path that is due to intermolecular transport. Figure 7 displays the histogram of this ratio for all cases along with basic statistics. The worst properties with this metric are for case 1-step 1; on average, 47% of the path are intermolecular hops. By thermal annealing, we observe that this fraction improves by 8% and decreases to 39% on average. The beneficial effect of annealing is consistent for other samples as well. In general, annealed samples show a lower fraction of intermolecular pathways. Interestingly, after returning to room temperature, this fraction does not deteriorate significantly. For case 2, this fraction worsens only by 4% on average. With both electrodes deposited (step 2), the best properties are reported for case 1, followed by cases 3 and 2, respectively. The smaller intermolecular fraction of case 1 can be another reason for the experimentally reported improved performance for these configuration. Similarly, the inverted architecture, case 3, shows superior metric as compared to the conventional configuration, case 2, again being consistent with experimental studies.[6,14] We note, however, that the differences in the mean fraction between samples are small, ∼1%. In conclusion, we note that while we currently only distinguish between interchain and intrachain transport pathways, it opens the possibility for further quantitative analysis. For instance, linking these graph-based results with quantum calculations of electronic couplings will provide relative weights for inter- and intramolecular transport. This will allow more quantitative analysis of transport.

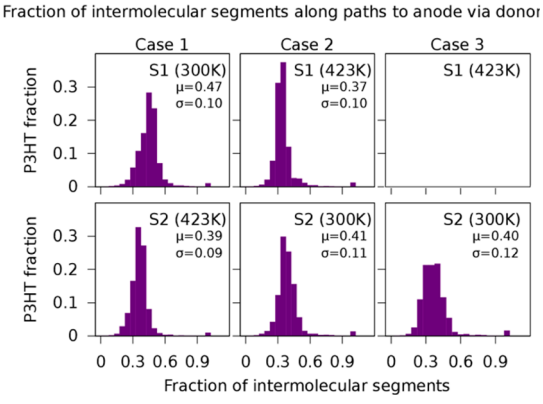

Figure 7. Fraction of intermolecular segments along the path to anode via donor.

4. CONCLUSIONS

In the present study, we developed a multiscale molecular simulation platform to study the effect of processing on the morphology with special emphasis on the link to the photovoltaic processes in organic solar cells. We focus on various configurations of electrode materials as well as sequence of annealing protocol (annealing before and after top electrode deposition). We first carry out a series of large-scale, coarse-grained molecular simulations to trace morphology evolution at device level. We next decode complex morphologies into a set of physically meaningful morphology features using a novel extension of our graph-based framework to quantify morphological features. We make the following observations:

(i) A thin P3HT-rich film is formed at free surface during thermal annealing.

(ii) Preferential segregation of P3HT chains and PCBM molecules toward PEDOT:PSS and Al electrodes, respectively, regardless of the sequence of electrode deposition.

(iii) Local depletion zones formed behind the enrichment outer layers on both ends of BHJ with comparable extent.

(iv) Orientation of polymer chains mildly sensitive to processing schedule.

These morphology-related trends were checked against the effect on the connectivity of domains, as well as quality of paths:

(i) Local depletion zone does not affect connectivity of domains toward preferential electrode. Well-connected and interpenetrated network forms regardless of local depletion zone.

(ii) Depletion zone has unfavorable effects on the distribution of path length. In particular, it leads to the deficiency of available transport pathways close to the electrode, just before charge collection (bottleneck for charge collection).

(iii) Only when sample is annealed with both electrodes deposited are paths well balanced.

(iv) Annealing improves the fraction of intermolecular segments along the shortest paths.

Finally, on the basis of the morphological features decoded from studied samples, we hypothesize reasons behind differences in performance between pre- and postdeposition annealing, as well as inverted and conventional configuration:

(i) Preannealing versus postannealing: Case 1 (postannealing) shows superior intermolecular fraction. Moreover, for case 1, we report perfect balance in transport pathway length distribution between hole and electron path lengths.

(ii) Inverted versus conventional architecture: Case 3 (inverted) shows superior intermolecular fraction as compared to conventional configuration.

We envision this study, combining multiscale molecular simulation framework with an extensive morphology feature analysis, as an important tool to establish a more detailed link between processing morphology and properties, thus providing rational pathways for process optimization. In particular, the coupled CGMD graph-based framework can be naturally applied to quantify various pressing problems in semiconducting polymer physics, like (a) the inherently multiscale nature of charge transport, and (b) quantifying the effect of molecular packing at the donor−acceptor interface.

■ ASSOCIATED CONTENT

Supporting Information

CG model potentials and parameters of PEDOT:PSS/P3HT:PCBM/Al device. Comparison between the CG model and atomistic model for the predicted pair interaction potential (for two like thin slabs constituted by aluminum), radial distribution functions (for all pair interactions), distribution functions of the bond length, bond angle, and planar angle (for PEDOT and PSS). Graph-based morphology quantification for atom-based morphology. This material is available free of charge via the Internet at http://pubs.acs.org.

■ AUTHOR INFORMATION

Corresponding Authors

*E-mail: baskarg@iastate.edu.

*E-mail: cwpao@gate.sinica.edu.tw.

Present Address

[⊥]Mechanical and Aerospace Engineering Department, University at Buffalo, Buffalo, NY 14260, United States

Author Contributions

[∥]Both authors contributed equally.

Notes

The authors declare no competing financial interest.

■ ACKNOWLEDGMENTS

C.-K.L. and C.-W.P. thank for the Research Center for Applied Science, Academia Sinica, Academia Sinica Thematic project no. AS-103-SS-A02, and the National Science Council of Taiwan (project nos. NSC 99-2112-M-001-004-MY3 and 102-2628-M-001-004-MY3) for financial support, and the National Center for High Performance Computing for computational support. C.-K.L. also is thankful for the support of the talent development program between Academia Sinica of Taiwan ROC and elite American universities and research institutes. O.W. and B.G. thank the National Science Foundation for partial support (NSF CAREER 1149365, NSF 1236839) and computing support via XSEDE (CTS110007). B.G. also thanks KAUST CRG for partial support.

■ REFERENCES

(1) Yang, X.; Loos, J.; Veenstra, S.; Verhees, W. J. H.; Wienk, M. M.; Kroon, J. M.; Michels, M. A. J.; Janssen, R. A. J. Nanoscale Morphology of High-Performance Polymer Solar Cells. *Nano Lett.* **2005**, *5*, 579−583.

(2) Klimov, E.; Li, W.; Yang, X.; Hoffmann, G. G.; Loos, J. Scanning Near-Field and Confocal Raman Microscopic Investigation of P3HT-PCBM Systems for Solar Cell Applications. *Macromolecules* **2006**, *39*, 4493−4496.

(3) van Bavel, S.; Sourty, E.; de With, G.; Frolic, K.; Loos, J. Relation between Photoactive Layer Thickness, 3D Morphology, and Device Performance in P3HT/PCBM Bulk-Heterojunction Solar Cells. *Macromolecules* **2009**, *42*, 7396−7403.

(4) Ballantyne, A. M.; Ferenczi, T. A. M.; Campoy-Quiles, M.; Clarke, T. M.; Maurano, A.; Wong, K. H.; Zhang, W.; Stingelin-Stutzmann, N.; Kim, J. S.; Bradley, D. D. C.; Durrant, J. R.; McCulloch, I.; Heeney, M.; Nelson, J. Understanding the Influence of Morphology on Poly(3-hexylselenothiophene):PCBM Solar Cells. *Macromolecules* **2010**, *43*, 1169−1174.

(5) Li, G.; Yao, Y.; Yang, H.; Shrotriya, V.; Yang, G.; Y, Y. "Solvent Annealing" Effect in Polymer Solar Cells Based on Poly(3-hexylthiophene) and Methanofullerenes. *Adv. Funct. Mater.* **2007**, *17*, 1636−1644.

(6) Xu, Z.; Chen, L. M.; Yang, G.; Huang, C. H.; Hou, J.; Wu, Y.; Li, G.; Hsu, C. S.; Yang, Y. Vertical Phase Separation in Poly(3-hexylthiophene): Fullerene Derivative Blends and its Advantage for Inverted Structure Solar Cells. *Adv. Funct. Mater.* **2009**, *19*, 1227−1234.

(7) Chen, H. Y.; Hou, J.; Zhang, S.; Liang, Y.; Yang, G.; Yang, Y.; Yu, L.; Wu, Y.; Li, G. Polymer Solar Cells with Enhanced Open-Circuit Voltage and Efficiency. *Nat. Photonics* **2009**, *3*, 649−653.

(8) Kumar, A.; Devine, R.; Mayberry, C.; Lei, B.; Li, G.; Yang, Y. Origin of Radiation-Induced Degradation in Polymer Solar Cells. *Adv. Funct. Mater.* **2010**, *20*, 2729−2736.

(9) Borchert, H. Elementary Processes and Limiting Factors in Hybrid Polymer/Nanoparticle Solar Cells. *Energy Environ. Sci.* **2010**, *3*, 1682−1694.

(10) Dennler, G.; Scharber, M. C.; Brabec, C. J. Polymer-Fullerene Bulk-Heterojunction Solar Cells. *Adv. Mater.* **2009**, *21*, 1323−1338.

(11) Kippelen, B.; Brédas, J.-L. Organic Photovoltaics. *Energy Environ. Sci.* **2009**, *2*, 251−261.

(12) Brabec, C. J.; Sariciftci, N. S.; Hummelen, J. C. Plastic Solar Cells. *Adv. Funct. Mater.* **2001**, *11*, 15−26.

(13) Mayer, A. C.; Scully, S. R.; Hardin, B. E.; Rowell, M. W.; McGehee, M. D. Polymer-Based Solar Cells. *Mater. Today* **2007**, *10*, 28−33.

(14) Liao, H. H.; Chen, L. M.; Xu, Z.; Li, G.; Yang, Y. Highly Efficient Inverted Polymer Solar Cell by Low Temperature Annealing of Cs2CO3 Interlayer. *Appl. Phys. Lett.* **2008**, *92*, 173303.

(15) Vaynzof, Y.; Kabra, D.; Zhao, L.; Chua, L. L.; Steiner, U.; Friend, R. H. Surface-Directed Dpinodal Fecomposition in Poly[3-hexylthiophene] and C61-Butyric Acid Methyl Ester Blends. *ACS Nano* **2011**, *5*, 329−336.

(16) Parnell, A. J.; Dunbar, A. D. F.; Pearson, A. J.; Staniec, P. A.; Dennison, A. J. C.; Hamamatsu, H.; Skoda, M. W. A.; Lidzey, D. G.; Jones, R. A. L. Depletion of PCBM at the Cathode Interface in P3HT/PCBM Thin Films as Quantified via Neutron Reflectivity Measurements. *Adv. Mater.* **2010**, *22*, 2444−2447.

(17) Campoy-Quiles, M.; Ferenczi, T.; Agostinelli, T.; Etchegoin, P. G.; Kim, Y.; Anthopoulos, T. D.; Stavrinou, P. N.; Bradley, D. D.; Nelson, J. Morphology Evolution via Self-Organization and Lateral and Vertical Diffusion in Polymer:Fullerene Solar Cell Blends. *Nat. Mater.* **2008**, *7*, 158−164.

(18) Chen, D.; Nakahara, A.; Wei, D.; Nordlund, D.; Russell, T. P. P3HT/PCBM Bulk Heterojunction Organic Photovoltaics: Correlating Efficiency and Morphology. *Nano Lett.* **2011**, *11*, 561−567.

(19) Wang, H.; Gomez, E. D.; Kim, J.; Guan, Z.; Jaye, C.; Fischer, D. A.; Kahn, A.; Loo, Y.-L. Device Characteristics of Bulk-Heterojunction

Polymer Solar Cells are Independent of Interfacial Segregation of Active Layers. *Chem. Mater.* **2011**, *23*, 2020−2023.
(20) Kim, J. B.; Kim, P.; Pégard, N. C.; Oh, S. J.; Kagan, C. R.; Fleischer, J. W.; Stone, H. A.; Loo, Y.-L. Wrinkles and Deep Folds as Photonic Structures in Photovoltaics. *Nat. Photonics* **2012**, *6*, 327−332.
(21) Kim, J. B.; Lee, S.; Toney, M. F.; Chen, Z.; Facchetti, A.; Kim, Y. S.; Loo, Y.-L. Reversible Soft-Contact Lamination and Delamination for Non-Invasive Fabrication and Characterization of Bulk-Heterojunction and Bilayer Organic Solar Cells. *Chem. Mater.* **2010**, *22*, 4931−4938.
(22) Huang, D. M. Computational Study of P3HT/C60-Fullerene Miscibility. *Aust. J. Chem.* **2014**, *67*, 585−591.
(23) Peter, C.; Kremer, K. Multiscale Simulation of Soft Matter Systems − from the Atomistic to the Coarse-Grained Level and Back. *Soft Matter* **2009**, *5*, 4357−4366.
(24) Lee, C. K.; Pao, C. W.; Chu, C. W. Multiscale Molecular Simulations of the Nanoscale Morphologies of P3HT:PCBM Blends for Bulk Heterojunction Organic Photovoltaic Cells. *Energy Environ. Sci.* **2011**, *4*, 4124−4132.
(25) Carrillo, J.-M. Y.; Kumar, R.; Goswami, M.; Sumpter, B. G.; Brown, W. M. New Insights into the Dynamics and Morphology of P3HT:PCBM Active Layers in Bulk Heterojunctions. *Phys. Chem. Chem. Phys.* **2013**, *15*, 17873−17882.
(26) To, T. T.; Adams, S. Modelling of P3HT:PCBM Interface Using Coarse-Grained Forcefield Derived from Accurate Atomistic Forcefield. *Phys. Chem. Chem. Phys.* **2014**, *16*, 4653−4663.
(27) Kipp, D.; Ganesan, V. Influence of Block Copolymer Compatibilizers on the Morphologies of Semiflexible Polymer/Solvent Blends. *J. Phys. Chem. B* **2014**, *118*, 4425−4441.
(28) Ganesan, V.; Jayaraman, A. Theory and Simulation Studies of Effective Interactions, Phase Behavior and Morphology in Polymer Nanocomposites. *Soft Matter* **2014**, *10*, 13−38.
(29) Dobrynin, A. V.; Carrillo, J.-M. Y.; Rubinstein, M. Chains Are More Flexible Under Tension. *Macromolecules* **2010**, *43*, 9181−9190.
(30) Kozub, D. R.; Vakhshouri, K.; Orme, L. M.; Wang, C.; Hexemer, A.; Gomez, E. D. Polymer Crystallization of Partially Miscible Polythiophene/Fullerene Mixtures Controls Morphology. *Macromolecules* **2011**, *44*, 5722−5726.
(31) Yin, W.; Dadmun, M. A New Model for the Morphology of P3HT/PCBM Organic Photovoltaics from Small-Angle Neutron Scattering: Rivers and Streams. *ACS Nano* **2011**, *5*, 4756−4768.
(32) Lee, C. K.; Pao, C. W. Solubility of [6,6]-Phenyl-C61-butyric Acid Methyl Ester and Optimal Blending Ratio of Bulk Heterojunction Polymer Solar Cells. *J. Phys. Chem. C* **2012**, *116*, 12455−12461.
(33) Xia, Y.; Sun, K.; Ouyang, J. Highly Conductive Poly(3,4-ethylenedioxythiophene):Poly(styrene sulfonate) Films Treated with an Amphiphilic Fluoro Compound as the Transparent Electrode of Polymer Solar Cells. *Energy Environ. Sci.* **2012**, *5*, 5325−5332.
(34) Bubnova, O.; Khan, Z. U.; Malti, A.; Braun, S.; Fahlman, M.; Berggren, M.; Crispin, X. Optimization of the Thermoelectric Figure of Merit in the Conducting Polymer Poly(3,4-ethylenedioxythiophene). *Nat. Mater.* **2011**, *10*, 429−433.
(35) Todorov, I. T.; Smith, W. *The DL_POLY_4 User Manual*; Daresbury Laboratory: Daresbury, 2011.
(36) Wodo, O.; Tirthapura, S.; Chaudhary, S.; Ganapathysubramanian, B. Modeling Morphology Evolution During Solventbased Fabrication of Organic Solar Cells. *Org. Electron.* **2012**, *13*, 1105−1113.
(37) Wodo, O.; Roehling, J. D.; Moule, A. J.; Ganapathsubramanian, B. Quantifying Organic Solar Cell Morphology: A Computational Study of Three-Dimensional Maps. *Energy Environ. Sci.* **2013**, *6*, 3060−3070.
(38) Wodo, O.; Tirthapura, S.; Chaudhary, S.; Ganapathysubramanian, B. A Computational Interrogation of Bulk Heterojunction Nanomorphology. *J. Appl. Phys.* **2012**, *12*, 06431.
(39) Dijkstra, E. A Note on Two Problems in Connexion with Graphs. *Numer. Math.* **1959**, *1*, 269−271.
(40) Cormen, T. H.; Leiserson, C. E.; Rivest, R. L.; Stein, C. *Introduction to Algorithms*; MIT Press: Cambridge, 2009.
(41) Müller, C.; Ferenczi, T. A. M.; Campoy-Quiles, M.; Frost, J. M.; Bradley, D. D. C.; Smith, P.; Stingelin-Stutzmann, N.; Nelson, J. Binary Organic Photovoltaic Blends: A Simple Rationale for Optimum Compositions. *Adv. Mater.* **2008**, *20*, 3510−3515.
(42) Pfannmöller, M.; Flügge, H.; Benner, G.; Wacker, I.; Sommer, C.; Hanselmann, M.; Schmale, S.; Schmidt, H.; Hamprecht, F. A.; Rabe, T.; Kowalsky, W.; Schröder, R. R. Visualizing a Homogeneous Blend in Bulk Heterojunction Polymer Solar Cells by Analytical Electron Microscopy. *Nano Lett.* **2011**, *11*, 3099−3107.
(43) Treat, N. D.; Brady, M. A.; Smith, G.; Toney, M. F.; Kramer, E. J.; Hawker, C. J.; Chabinyc, M. L. Interdiffusion of PCBM and P3HT Reveals Miscibility in a Photovoltaically Active Blend. *Adv. Energy Mater.* **2011**, *1*, 82−89.
(44) Collins, B. A.; Gann, E.; Guignard, L.; He, X.; McNeill, C. R.; Ade, H. Molecular Miscibility of Polymer-Fullerene Blends. *J. Phys. Chem. Lett.* **2010**, *1*, 3160−3166.
(45) Vandewal, K.; Himmelberger, S.; Salleo, A. Structural Factors That Affect the Performance of Organic Bulk Heterojunction Solar Cells. *Macromolecules* **2013**, *46*, 6379−6387.
(46) Germack, D. S.; Chan, C. K.; Kline, R. J.; Fischer, D. A.; Gundlach, D. J.; Toney, M. F.; Richter, L. J.; DeLongchamp, D. M. Interfacial Segregation in Polymer/Fullerene Blend Films for Photovoltaic Devices. *Macromolecules* **2010**, *43*, 3828−3836.
(47) Ajuria, J.; Etxebarria, I.; Cambarau, W.; Munecas, U.; Tena-Zaera, R.; Jimenoc, J. C.; Pacios, R. Inverted ITO-Free Organic Solar Cells Based on P and N Semiconducting Oxides. New Designs for Integration in Tandem Cells, Top or Bottom Detecting Devices, and Photovoltaic Windows. *Energy Environ. Sci.* **2011**, *4*, 453−458.
(48) Cheun, H.; Berrigan, J. D.; Zhou, Y.; Fenoll, M.; Shim, J.; Fuentes-Hernandez, C.; Sandhage, K. H.; Kippelen, B. Roles of Thermally-Induced Vertical Phase Segregation and Crystallization on the Photovoltaic Performance of Bulk Heterojunction Inverted Polymer Solar Cells. *Energy Environ. Sci.* **2011**, *4*, 3456−3460.
(49) DeLongchamp, D. M.; Kline, R. J.; Herzing, A. Nanoscale Structure Measurements for Polymer-Fullerene Photovoltaics. *Energy Environ. Sci.* **2012**, *5*, 5980−5993.
(50) Wang, H.; Shah, M.; Ganesan, V.; Chabinyc, M. L.; Loo, Y.-L. Tail State-Assisted Charge Injection and Recombination at the Electron-Collecting Interface of P3HT:PCBM Bulk-Heterojunction Polymer Solar Cells. *Adv. Energy Mater.* **2012**, *2*, 1447−1455.
(51) Germack, D. S.; Chan, C. K.; Hamadani, B. H.; Richter, L. J.; Fischer, D. A.; Gundlach, D. J.; DeLongchamp, D. M. Substrate-Dependent Interface Composition and Charge Transport in Films for Organic Photovoltaics. *Appl. Phys. Lett.* **2009**, *94*, 233303.
(52) Mauger, S. A.; Chang, L.; Friedrich, S.; Rochester, C. W.; Huang, D. M.; Wang, P.; Moulé, A. J. Self-Assembly of Selective Interfaces in Organic Photovoltaics. *Adv. Funct. Mater.* **2013**, *23*, 1935−1946.
(53) Alam, M. A.; Ray, B.; Khan, M. R.; Dongaonka, S. The Essence and Efficiency Limits of Bulk-Heterostructure Organic Solar Cells: A Polymerto-Panel Perspective. *J. Mater. Res.* **2013**, *28*, 541−557.
(54) Noriega, R.; Salleo, A.; Spakowitz, A. J. Chain Conformations Dictate Multiscale Charge Transport Phenomena in Disordered Semiconducting Polymers. *Proc. Natl. Acad. Sci. U.S.A.* **2013**, *110*, 16315−16320.
(55) Devizis, A.; Meerholz, K.; Hertel, D.; Gulbinas, V. Hierarchical Charge Carrier Motion in Conjugated Polymers. *Chem. Phys. Lett.* **2010**, *498*, 302−306.
(56) Laquai, F.; Wegner, G.; Bässler, H. What Determines the Mobility of Charge Carriers in Conjugated Polymers? *Philos. Trans. R. Soc., A* **2007**, *365*, 1473−1487.